PNAS RESEARCH ARTICLE | CHEMISTRY

Revealing the roles of the solid–electrolyte interphase in designing stable, fast-charging, low-temperature Li-ion batteries

Lei Tao[a,1], Hanrui Zhang[b,1], Sameep Rajubhai Shah[c,1], Xixian Yang[c], Jianwei Lai[b], Yanjun Guo[b], Joshua A. Russell[d], Dawei Xia[a], Jungki Min[a], Weibo Huang[a], Chenguang Shi[a], Zhaohui Liang[a], Deyang Yu[a], Sooyeon Hwang[e], Hui Xiong[d], Louis A. Madsen[a,f], Kejie Zhao[c,2], Feifei Shi[b,2], and Feng Lin[a,f,g,2]

Affiliations are included on p. 9.

Edited by Peidong Yang, University of California, Berkeley, CA; received October 4, 2024; accepted February 11, 2025

Designing the solid–electrolyte interphase (SEI) is critical for stable, fast-charging, low-temperature Li-ion batteries. Fostering a "fluorinated interphase," SEI enriched with LiF, has become a popular design strategy. Although LiF possesses low Li-ion conductivity, many studies have reported favorable battery performance with fluorinated SEIs. Such a contradiction suggests that optimizing SEI must extend beyond chemical composition design to consider spatial distributions of different chemical species. In this work, we demonstrate that the impact of a fluorinated SEI on battery performance should be evaluated on a case-by-case basis. Sufficiently passivating the anode surface without impeding Li-ion transport is key. We reveal that a fluorinated SEI containing excessive and dense LiF severely impedes Li-ion transport. In contrast, a fluorinated SEI with well-dispersed LiF (i.e., small LiF aggregates well mixed with other SEI components) is advantageous, presumably due to the enhanced Li-ion transport across heterointerfaces between LiF and other SEI components. An electrolyte, 1 M $LiPF_6$ in 2-methyl tetrahydrofuran (2MeTHF), yields a fluorinated SEI with dispersed LiF. This electrolyte allows anodes of graphite, μSi/graphite composite, and pure Si to all deliver a stable Coulombic efficiency of 99.9% and excellent rate capability at low temperatures. Pouch cells containing layered cathodes also demonstrate impressive cycling stability over 1,000 cycles and exceptional rate capability down to −20 °C. Through experiments and theoretical modeling, we have identified a balanced SEI-based approach that achieves stable, fast-charging, low-temperature Li-ion batteries.

fluorinated interphase | dispersed LiF | Li-ion transport | weakly solvating electrolyte | extreme condition

Significance

The "fluorinated interphase" is often seen as a catch-all solution for enhancing battery performance, despite LiF having a high Li-ion diffusion barrier. This study emphasizes evaluating its effects case-by-case. We developed weakly solvating electrolytes to tailor solid–electrolyte interphase (SEI) microstructures for fast-charging and low-temperature Li-ion batteries. Our work focuses on the role of LiF size and distribution in regulating Li-ion diffusion. Experimental results reveal that a fluorine-rich SEI with excessive, dense LiF impedes Li-ion transport, whereas a dispersed LiF-based SEI favors battery performance. Physics-based finite element simulations further elucidate how an optimized SEI microstructure facilitates charge transport across the electrode, offering a feasible approach to better batteries in extreme environments.

Lithium-ion batteries (LIBs) have revolutionized the landscape of portable electronics and electric mobility. However, they still face challenges such as short lifespan under fast-charging, low-temperature conditions (1–4). These limitations intricately relate to Li-ion transport within the electrolyte and electrode, as well as across the interfaces (5–9). Specifically, Li-ion transport encompasses migration and diffusion in the bulk electrolyte, desolvation near the electrode surface, diffusion through the electrode-electrolyte interphase, and diffusion within the electrode (as depicted in Scheme 1) (9–11). Each step has a distinct energy barrier. Researchers have attributed the rate-limiting factors to the desolvation and SEI diffusion processes (10, 12–14). The physicochemical properties of the electrolyte can have major impacts on these steps.

Recent efforts have focused on tuning the solvation structure of electrolytes. For example, several studies applied weakly solvating electrolytes to expedite the desolvation process of Li ions (15–18). However, what has often been overlooked is whether the resulting SEI impedes or enhances Li-ion transport. Even if the desolvation energy barrier remains constant, the resulting components and distributions of the SEI can vary and profoundly influence Li-ion transport. Variations of SEI ultimately lead to the observed differences in electrochemical performance (19–22). Furthermore, there have been controversies over SEI functions. For example, LiF-rich SEI, often contributed by the decomposition of F-containing anions or fluorinated additives, is believed to conduct Li-ion rapidly in some papers (17, 18, 23–25). This contradicts some theoretical reports that LiF has a high Li-ion diffusion barrier (26, 27). We hypothesize that the critical determinant of this phenomenon lies not only in the SEI composition but also in the distributions of chemical species in the SEI.

Competing interest statement: Virginia Tech filed a US provisional patent application on the basis of this work. F.L. has a financial interest in Fermi Energy, Inc., which is licensing this technology.

This article is a PNAS Direct Submission.

[1]L.T., H.Z., and S.R.S. contributed equally to this work.

[2]To whom correspondence may be addressed. Email: kjzhao@purdue.edu, feifeishi@psu.edu, or fenglin@vt.edu.

This article contains supporting information online at https://www.pnas.org/lookup/suppl/doi:10.1073/pnas.2420398122/-/DCSupplemental.

Published March 24, 2025.

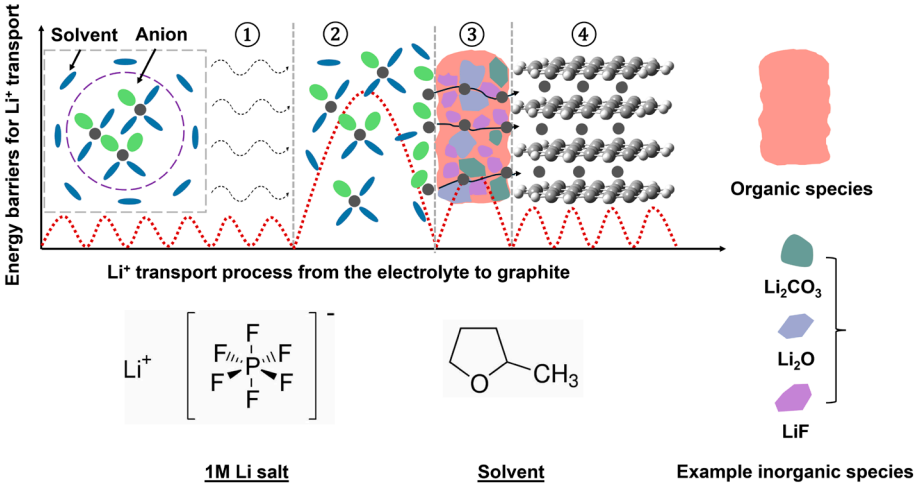

Scheme 1. The Li-ion transport process from the electrolyte to the graphite anode includes (1) migration and diffusion in the bulk electrolyte, (2) desolvation at the interface, (3) diffusion through the SEI layer, and (4) diffusion in the graphite anode. Each step corresponds to a distinct energy barrier (Y-axis), which is schematically represented by the red dashed line. Our 1 M $LiPF_6$-2MeTHF electrolyte is a weakly solvating electrolyte (easy desolvation) and possesses the contact ion pair (CIP)-dominant solvation structure, leading to the formation of a fluorinated SEI with a dispersed LiF distribution, favoring rapid Li-ion transport through SEI. Examples of some inorganic species in the SEI are schematically shown. In this work, the LiF content and distribution are controlled by modifying a fluorinated additive or a salt.

To test our hypothesis, we systematically designed a series of weakly solvating electrolytes at a 1 M salt concentration to vary SEI compositions and distributions of chemical species in the SEI. Through experimental analyses and computational modeling, we have identified the pivotal role of the size and distribution of LiF aggregates in determining Li-ion transport through the SEI, especially during fast charging at low temperatures. Our results highlight the advantage of smaller, dispersed LiF aggregates for efficiently passivating the electrode surface and promoting favorable Li-ion transport. We demonstrated that cyclic ether-based electrolyte (1 M $LiPF_6$ in 2-methyl tetrahydrofuran, 2MeTHF, Scheme 1) exhibits excellent fast charging performance in various anodes (graphite, μSi/graphite, and Si) and has outstanding rate capability at −20 °C.

Results and Discussion

Solvation Structure of the Electrolyte at Different Temperatures. Three electrolytes, namely 1 M $LiPF_6$-2MeTHF, 1 M LiFSI-2MeTHF, and 1 M $LiPF_6$-2MeTHF+2vol.% FEC, are compared in this work. The composition of the SEI is controlled by changing Li salt or adding FEC additive. Raman spectra indicate that Li^+ in all three electrolytes is coordinated with 2MeTHF, exhibiting the same characteristic bond of Li^+-2MeTHF near 922 cm^{-1} (Fig. 1*A* and *SI Appendix*, Fig. S1*A*). Among the three electrolytes, the shift of the characteristic 2MeTHF at 919 cm^{-1} is marginally smaller in 1 M $LiPF_6$-2MeTHF (+2 cm^{-1}) than those in 1 M LiFSI-2MeTHF (+3 cm^{-1}) and 1 M $LiPF_6$-2MeTHF+2vol.% FEC (+4 cm^{-1}). Thus, the Li^+-2MeTHF interaction is the weakest in 1 M $LiPF_6$-2MeTHF. Additionally, when the temperature is lowered to −20 °C, the solvation structures of the three electrolytes do not change significantly due to the low melting point of the 2MeTHF solvent (Fig. 1*A* and *SI Appendix*, Fig. S1*A*). FTIR results confirm clear CIP peaks in the three electrolytes (Fig. 1*B* and *SI Appendix*, Fig. S1*B*). The C-O-C in 2MeTHF coordinates with Li^+ after introducing salts. The proportion of 2MeTHF participating in Li^+ solvation is 35% in 1 M $LiPF_6$-2MeTHF, 34% in 1 M $LiPF_6$-2MeTHF+2vol.% FEC, and 37% in 1 M LiFSI-2MeTHF (Fig. 1*B* and *SI Appendix*, Fig. S1*B*). Based on NMR diffusometry experiments, the diffusion coefficients of Li^+ and anions (PF_6^-/FSI^-) are synchronized in the electrolytes (*SI Appendix*, Fig. S2 and Table S1), and the calculated Haven ratios are much larger than 1 (in the range of 5 to 18, *SI Appendix*, Fig. S2*D*), indicating the cations and anions are diffusing together in the form of ion pairs and clusters (28), characteristic of an electrolyte rich in CIP.

MD simulations are conducted to gain insights into the solvation structures of the three electrolytes. The RDFs and CNs between Li^+, anions, and 2MeTHF in the three electrolytes at 296 K (23 °C) are depicted. The RDFs show that both solvent (2MeTHF) and anions (PF_6, FSI^-) are involved in the formation of Li^+ primary solvation sheath in three electrolytes (Fig. 1*C* and *SI Appendix*, Fig. S1*C*). In the 1 M $LiPF_6$-2MeTHF electrolyte, 2MeTHF solvent and PF_6^- anion are tightly packed around Li^+ with the first peak position at 2.3 and 2.5 Å, respectively. The corresponding CNs of the first sheath of Li^+ are 3.03 and 2.09 for Li^+/2MeTHF and Li^+/PF_6^-, indicating that plenty of PF_6^- appear in the first sheath coordinating with Li^+ (Fig. 1*C*). After adding 2vol.% FEC, it still shows the same RDF peak position, and the Li^+/FEC CN in the Li^+ first coordination sheath is only 0.03, indicating that 2vol.% FEC does not change the main solvation structure (*SI Appendix*, Fig. S1 *C*, *Left*). In 1 M LiFSI-2MeTHF, the first RDF peak of Li^+/2MeTHF and Li^+/FSI^- is 2.3 and 2.5 Å, which are the same as in $LiPF_6$-based electrolytes. However, the first RDF peak of Li^+/FSI^- is more pronounced than that of Li^+/2MeTHF (*SI Appendix*, Fig. S1 *C*, *Right*), indicating more anions in the Li^+ first coordination sheath than in $LiPF_6$-based electrolytes. Apart from RDFs and CNs, statistical analysis is carried out to identify solvent-separated ion pair (SSIP), CIP, and aggregate (AGG) in the three electrolytes. The 1 M $LiPF_6$-2MeTHF electrolyte has 16% SSIP, 63% CIP, and 21% AGG (Fig. 1*E*), while adding 2vol.% FEC leads to 21% SSIP, 61% CIP, and 18% AGG, close to 1 M $LiPF_6$-2MeTHF (*SI Appendix*, Fig. S1 *C*, *Left*). This statistical result is consistent with the RDFs and CNs results, corroborating a slight difference between the 1 M $LiPF_6$-2MeTHF electrolyte with and without FEC. The 1 M LiFSI-2MeTHF electrolyte contains 10% SSIP, 44% CIP, and 46% AGG, with more AGG structures explaining the larger CN between Li^+ and anion than that in $LiPF_6$-based electrolytes (*SI Appendix*, Fig. S1 *C*, *Right*). These results indicate that the three electrolytes have weakly solvating structures, so the anion decomposition will mainly contribute to the main inorganic component of the SEI, with more anion decomposition happening in the 1 M LiFSI-2MeTHF electrolyte. When cooled to 253 K (−20 °C), there is no discernible change in the peak positions of RDFs of all three electrolytes (Fig. 1*D* and *SI Appendix*, Fig. S1*D*). The statistical results of SSIP, CIP, and AGG do not show a major difference between 253 and 296 K (Fig. 1*F* and *SI Appendix*, Fig. S1*D*). Therefore, these observations indicate that the solvation structures of three electrolytes do not alter much between 296 and 253 K.

Li-Ion Transport at Low Temperatures and Fast Charging. Graphite (Gr) displays obvious Li intercalation plateaus, facilitating the observation of Li-ion transport behavior. The intercalation

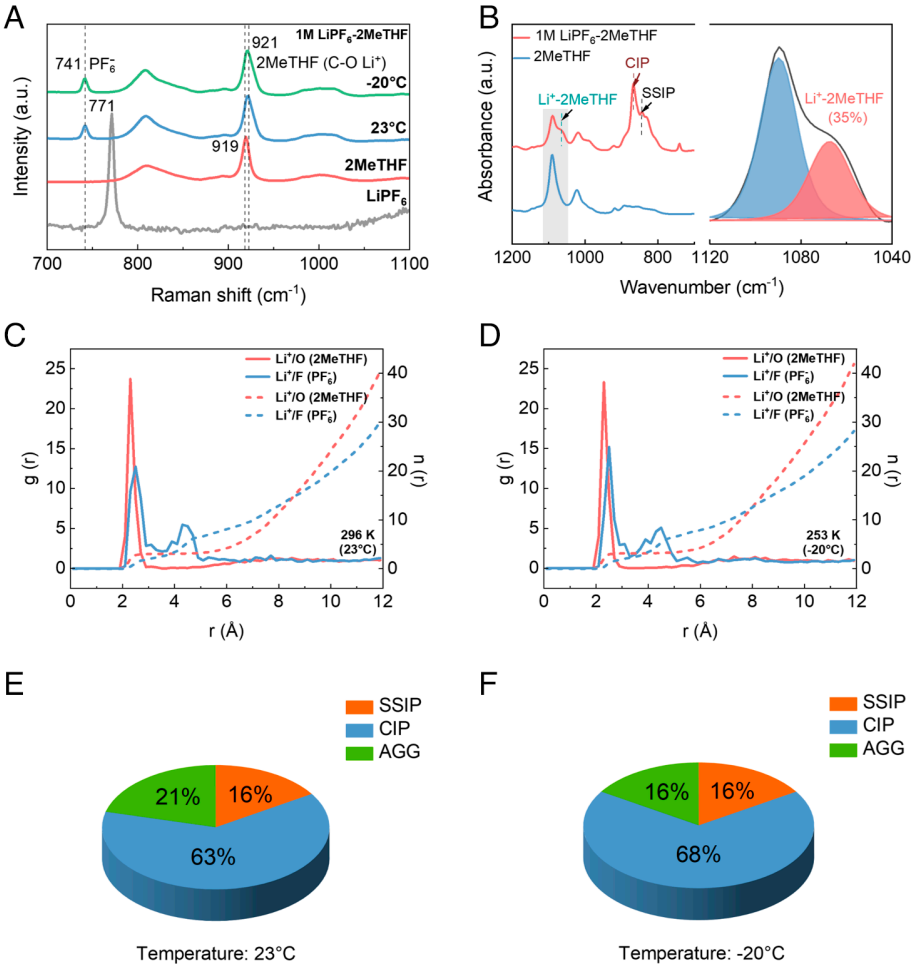

Fig. 1. Electrolyte properties at different temperatures. (*A*) Raman spectra of the 1 M $LiPF_6$-2MeTHF electrolyte at 23 and −20 °C, with $LiPF_6$ and 2MeTHF reference spectra included. As the temperature decreases, the representative peaks have not shifted. (*B*) FTIR spectra of the 1 M $LiPF_6$-2MeTHF electrolyte at 23 °C. In the fitted curves, blue represents free 2MeTHF solvent, and red represents Li^+ solvated by 2MeTHF (i.e., Li^+-2MeTHF). The proportion of 2MeTHF participating in Li^+ solvation is 35%. (*C* and *D*) Radial distribution function [RDF, g(r), solid] and coordination number [CN, n (r), dashed line] of oxygen and fluorine around Li^+ as a function of distance (r) from molecular dynamics (MD) simulations of the 1 M $LiPF_6$-2MeTHF electrolyte at 296 K (23 °C) and 253 K (−20 °C), respectively. (*E* and *F*) The corresponding statistical analysis of the most dominant Li^+ solvates (SSIP, CIP, and AGG) in the electrolyte at 23 °C (*E*) and −20 °C (*F*) from the MD simulations.

plateaus will be observed only if when Li ions go through the SEI and get intercalated. The parameters of graphite laminates are shown in *SI Appendix*, Table S2. Three electrolytes are tested in the graphite (Gr)||Li cells at 0.2 C (1 C = 0.37 A g^{-1}) within a temperature range from 23 to −20 °C (Fig. 2*A*). Graphite shows similar capacities of ~370 mAh g^{-1} using all electrolytes at 23 °C. As the temperature drops, graphite maintains a high reversible capacity using the 1 M $LiPF_6$-2MeTHF electrolyte even at −20 °C. However, the capacities decrease significantly using the other two electrolytes, especially from 0 to −20 °C. Corresponding voltage profiles show no plateau capacity at −20 °C, indicating virtually no Li-ion is intercalated into the graphite interlayer (Fig. 2*C*). The rate performance at room temperature is shown in Fig. 2*B*. The graphite anode exhibits a substantial capacity drop when cycled using the 1 M $LiPF_6$-2MeTHF+2vol.% FEC and 1 M LiFSI-2MeTHF electrolytes as the current increases from 1 to 5 C (a representative voltage profile at 2 C is shown in Fig. 2*D*). These results demonstrate the different Li-ion transport behavior in the three electrolytes under fast charging and low-temperature conditions. When incorporating the 1 M $LiPF_6$-2MeTHF electrolyte, Li-ion intercalation behavior still occurs at −20 °C, and Li-ion transport is not impeded, but it is impeded using the other two electrolytes. So, the following question arises: What factors limit the Li-ion intercalation in graphite under fast charging and low-temperature conditions? Three electrolytes show ionic conductivity at the same order of magnitude and similar fluidity within a temperature range from 20 to −40 °C (*SI Appendix*, Fig. S3). In addition, the 1 M LiFSI-2MeTHF electrolyte shows similar ionic conductivity as the 1 M $LiPF_6$-2MeTHF electrolyte across the temperature range. Thus, the Li-ion transport limitation in the bulk electrolyte cannot be a primary factor. Since Li ions intercalate into the graphite to form LiC_6 in all electrolytes at 23 °C (Fig. 2*A*) and Li ions can intercalate into graphite in the 1 M $LiPF_6$-2MeTHF electrolyte at −20 °C, the Li-ion diffusion limitation within the graphite interlayer is also negligible. Thus, the only limitations for Li-ion transport are desolvation and diffusion through the SEI layer.

To gain more information on electrolyte and SEI behaviors, ion transport behavior can be reflected in the interfacial kinetics analysis. Electrochemical impedance spectroscopy (EIS) reflects diverse ion transport behaviors in the three electrolytes during graphite lithiation at different temperatures. The semicircle in the mid-frequency region of the Nyquist plot represents the charge-transfer impedance (R_{ct}), and the semicircle in the high-frequency region represents Li-ion transport through the SEI (R_{SEI}) (*SI Appendix*, Fig. S4) (11, 29). Temperature-dependent EIS is employed to determine the kinetics of different interfacial processes. A three-electrode cell is designed for testing to reveal the impedance signal of the graphite electrode (*SI Appendix*, Fig. S5 *A* and *B*). *SI Appendix*, Fig. S5 *C–E* shows the impedance of Gr||Li cells at 50% lithiated state in different electrolytes at different temperatures. The overall impedance in the 1 M $LiPF_6$-2MeTHF electrolyte shows the lowest values at various temperatures, implying fast Li^+ reaction kinetics (*SI Appendix*, Fig. S5 *C–E* and Table S3). Specifically, as the temperature decreases, R_{SEI} increases significantly in 1 M $LiPF_6$-2MeTHF+2vol.% FEC (Fig. 2*E* and *SI Appendix*, Table S3). From 23 to −20 °C, R_{SEI} increases 10-fold in the 1 M $LiPF_6$-2MeTHF, 15-fold in the 1 M LiFSI-2MeTHF and 34-fold in the 1 M $LiPF_6$-2MeTHF+2vol.% FEC, respectively (*SI Appendix*, Table S3). The resistances are fitted according to the Arrhenius equation, and then the activation energy of each

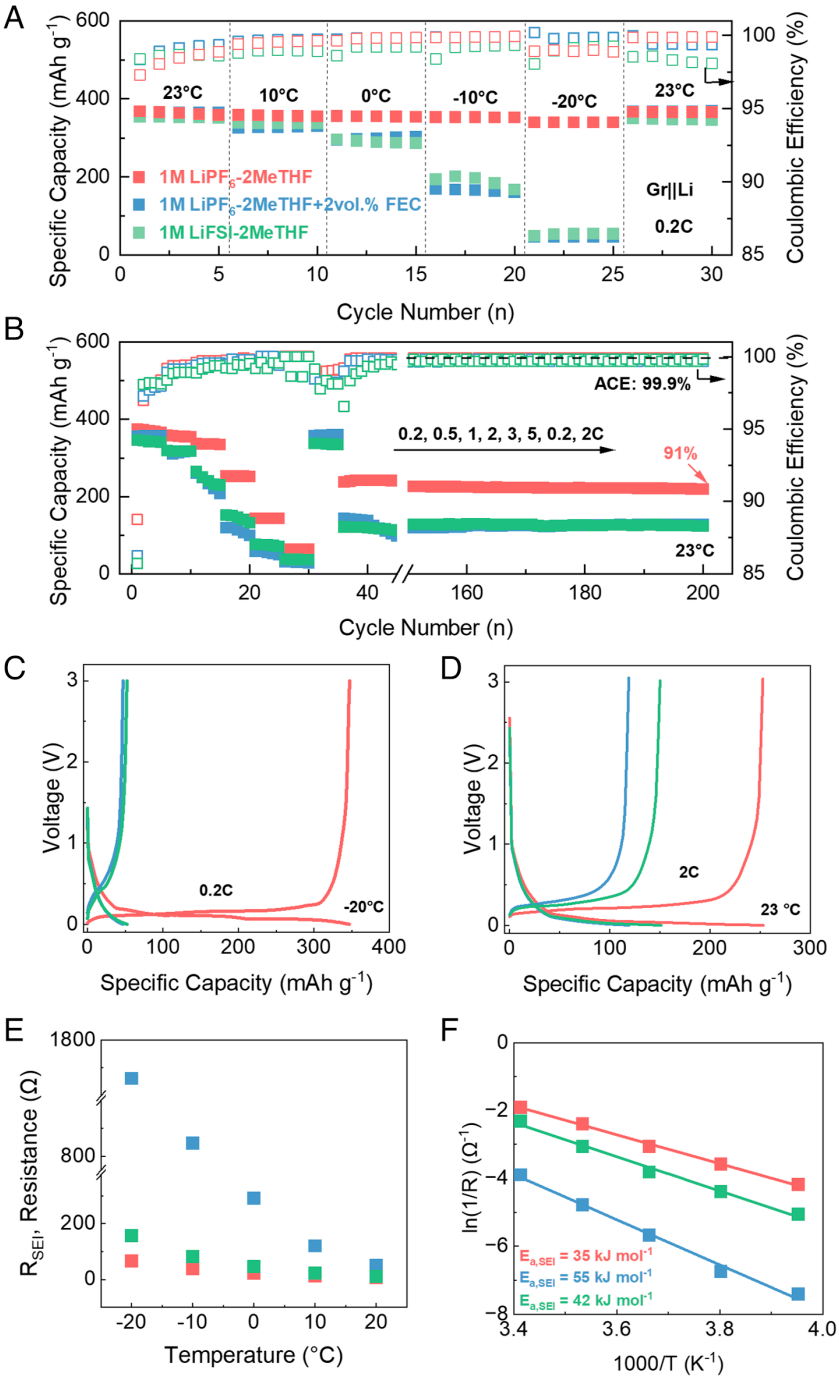

Fig. 2. Li-ion transport in the graphite cell at low temperatures and fast charging. (*A*) Graphite (Gr)||Li cells cycled using the three electrolytes (1 M $LiPF_6$-2MeTHF, 1 M $LiPF_6$-2MeTHF+2vol.% FEC, and 1 M LiFSI-2MeTHF) at temperatures from 23 to −20 °C. (*B*) Rate performance of the Gr||Li cell cycled in the three electrolytes at 23 °C. (*C*) Voltage profiles of the Gr||Li cell cycled in the three electrolytes at −20 °C. (*D*) Representative voltage profile of the Gr||Li cell cycled in the three electrolytes at 2 C and 23 °C. (*E*) Fitting results of R_{SEI} evolution at different temperatures. (*F*) Arrhenius plots and activation energies of R_{SEI} derived from temperature-dependent EIS measurements. All the figures share the same color scheme as shown in *A*.

interfacial process is obtained (9). The Li^+ desolvation energy barriers ($E_{a,ct}$) of three electrolytes are 42, 48, and 43 kJ mol^{-1}, respectively (*SI Appendix*, Fig. S6). The discrepancy in R_{ct} values is quite small. In contrast, the activation energy for Li-ion transport through the SEI ($E_{a,SEI}$) shows a large difference between the three electrolytes, 35, 55, and 42 kJ mol^{-1} for 1 M $LiPF_6$-2MeTHF, 1 M $LiPF_6$-2MeTHF+2vol.% FEC, and 1 M LiFSI-2MeTHF, respectively (Fig. 2*F*). The activation energy values are all close to the results calculated in the literature (15, 30). These results suggest that the SEI properties govern the Li-ion intercalation in graphite under fast charging and low-temperature conditions.

SEI Structure and Component Characterization and Analysis. Cyclic voltammetry (CV) curves reveal the SEI formation in different electrolytes (*SI Appendix*, Fig. S7). Obvious reduction peaks at high potentials are shown in the 1 M $LiPF_6$-2MeTHF+2vol.% FEC and 1 M LiFSI-2MeTHF electrolytes, corresponding to the decomposition of FEC additives and LiFSI salt, respectively (*SI Appendix*, Fig. S7 *B* and *C*). In contrast, a weak reduction peak related to the $LiPF_6$ decomposition is detected at a low potential in the 1 M $LiPF_6$-2MeTHF electrolyte (*SI Appendix*, Fig. S7*A*). These results indicate that the FEC additives and LiFSI salt exhibit poorer reduction stability. Thus, they decompose at earlier lithiation stages, producing more LiF reduction products (further details are discussed in supporting information). Cryo-TEM further investigates disparities in the distribution of SEI components. In the 1 M $LiPF_6$-2MeTHF electrolyte, the SEI is thin covering the graphite surface, accompanied by small crystallites distributed therein (Fig. 3*A*). In contrast, a continuous and dense SEI layer is observed in the 1 M $LiPF_6$-2MeTHF+2vol.% FEC

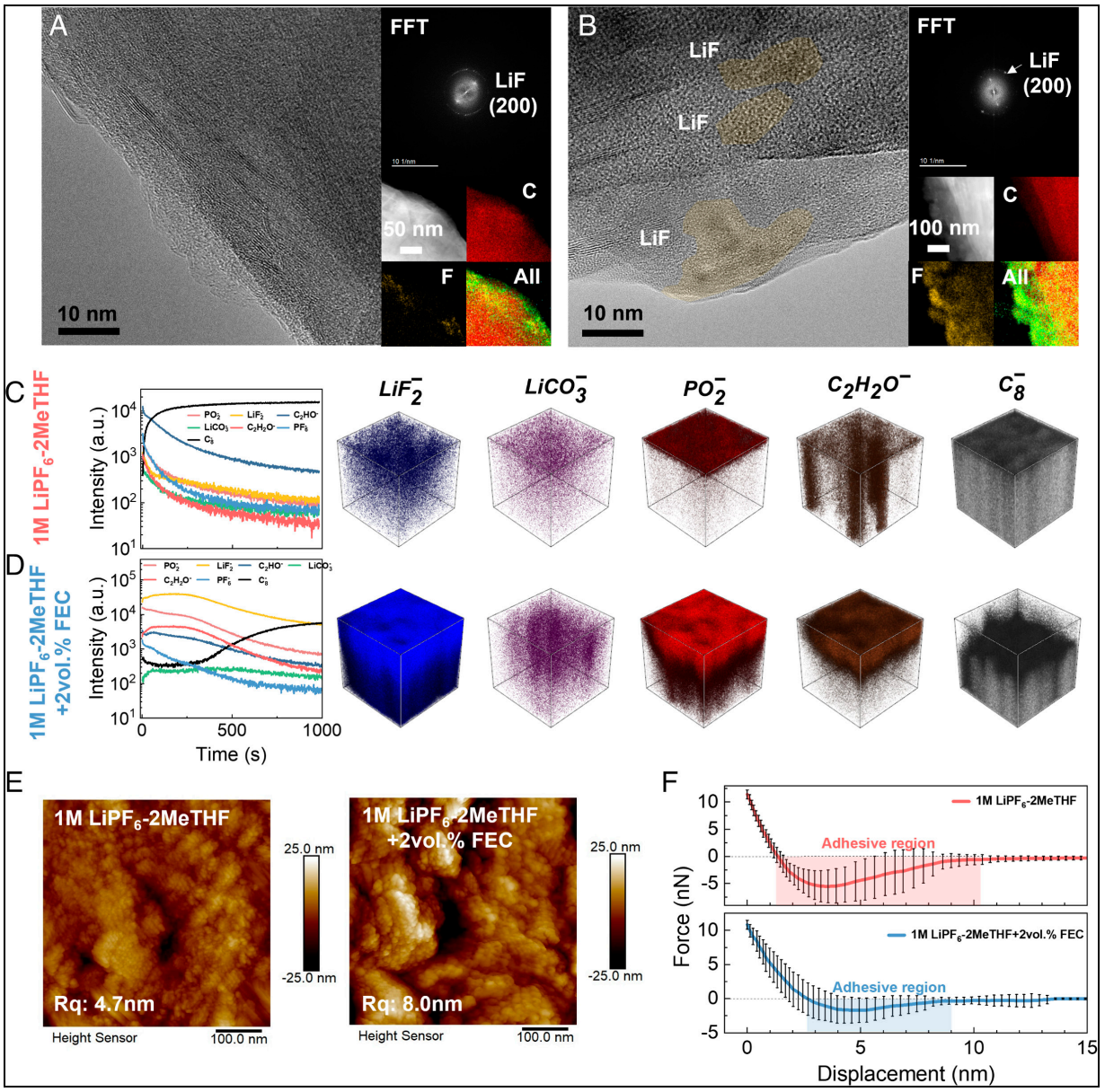

Fig. 3. SEI characterization. Cryo-TEM images of the graphite electrode cycled using (*A*) 1 M $LiPF_6$-2MeTHF and (*B*) 1 M $LiPF_6$-2MeTHF+2vol.% FEC electrolytes for 20 cycles, including the corresponding fast Fourier transform patterns and STEM-EDS elemental mapping of F, C, and elements overlaid in one image. TOF-SIMS depth profiles of various chemical species for the graphite anode using (*C*) 1 M $LiPF_6$-2MeTHF and (*D*) 1 M $LiPF_6$-2MeTHF+2vol.% FEC electrolytes after 20 cycles: 3D maps showing the distribution of several molecular fragments: LiF_2^-, $LiCO_3^-$, PO_2^-, $C_2H_2O^-$, and C_8^- in the graphite anode cycled using 1 M $LiPF_6$-2MeTHF and 1 M $LiPF_6$-2MeTHF+2vol.% FEC electrolytes, where the sample volume is a 100 × 100 μm area with a 100 nm depth. (*E*) The AFM surface roughness of the cycled graphite. (*F*) Force–displacement approach curves of AFM probe toward the SEI formed in the 1 M $LiPF_6$-2MeTHF and 1 M $LiPF_6$-2MeTHF+2vol.% FEC after 20 cycles, showing the thinner and less inorganic SEI layer in the former electrolyte, and the thicker and inorganic-rich SEI layer in the latter electrolyte. The error bars are created based on the SD of 40 independent measurements.

and 1 M LiFSI-2MeTHF electrolytes, along with larger crystallites (Fig. 3*B* and *SI Appendix*, Fig. S8). Fast Fourier transform (FFT) analysis reveals that all crystallites belong to LiF (Fig. 3 *A* and *B* and *SI Appendix*, Fig. S8). EDS mapping shows that the F signal is thin and well dispersed in the 1 M $LiPF_6$-2MeTHF electrolyte but becomes thicker and denser in the two other electrolytes (Fig. 3 *A* and *B* and *SI Appendix*, Fig. S8). Time-of-flight secondary ion mass spectrometry (ToF-SIMS) is employed to reconstruct some representative chemical fragments detected for the SEIs (Fig. 3 *C* and *D*). The SEI layer in the 1 M $LiPF_6$-2MeTHF electrolyte appears sporadically on the graphite surface, with the LiF^-_2 fragment loosely distributed across the graphite electrode (Fig. 3*C*). Conversely, a dense SEI layer is detected in the 1 M $LiPF_6$-2MeTHF+2vol.% FEC and 1 M LiFSI-2MeTHF electrolytes, where there is an enrichment of LiF^-_2 on the graphite surface (Fig. 3*D* and *SI Appendix*, Fig. S9). Such a difference implies that the distribution and size of LiF aggregates could limit Li-ion intercalation behavior. The roughness and mechanical properties of the formed SEI are probed by AFM (Fig. 3*E*). The roughness of the SEI formed in the 1 M $LiPF_6$-2MeTHF+2vol.% FEC electrolyte is 1.7 times that of the 1 M $LiPF_6$-2MeTHF electrolyte. The force-distance curve taken upon AFM nanoindentation of the 1 M $LiPF_6$-2MeTHF sample shows a wider adhesive region (negative force values) than the 1 M $LiPF_6$-2MeTHF+2vol.% FEC sample, signifying a softer, polymeric nature at the surface in the former. Then, it experiences a rapid increase after ~3.5 nm due to the presence of the inorganic inner layer. In contrast, the SEI formed in the 1 M $LiPF_6$-2MeTHF+2vol.% FEC electrolyte has a stiffer and thicker inorganic region. These AFM results are consistent with the analyses of TEM and ToF-SIMS.

Modeling of Intercalation Barriers for Li-Ion Transport. We perform finite element simulations to gain a deeper understanding of the impact of SEI on Li-ion intercalation and cell performance for the three electrolytes. Fig. 4*A* presents the 3D Gr||Li half-cell model developed for these simulations. The model geometry is ensured to have the same electrode thickness, mass loading, porosity, and active/inactive mass fractions as the graphite electrodes prepared for experimental characterization (*SI Appendix*, Table S2). The graphite electrode is created by randomly distributed plate-type graphite particles embedded in a porous matrix of inactive material. The electrolyte in the pore phase of the matrix provides interconnected channels for Li ion diffusion. A coupled electrochemical-mechanical theoretical framework is implemented over the 3D model geometry. Specifically, Li-ion intercalation is governed by the interfacial charge transfer reaction defined at each graphite–electrolyte interface. To ensure the reliability of our modeling, we did not tweak our simulation parameters, and we used experimental data, including equilibrium voltage (*SI Appendix*, Fig. S10), resistance (*SI Appendix*, Fig. S11), diffusivity (*SI Appendix*, Fig. S2 *B* and *C*), and conductivity (*SI Appendix*, Fig. S3*A*) as the direct inputs for the finite element simulations. To mimic the electrochemical losses incurred due to Li-ion transport across the SEI, temperature and lithiation degree-dependent R_{SEI} from EIS measurements are applied as film resistance at the interfaces. As shown in *SI Appendix*, Fig. S11 *A*–*C* and Table S4, R_{SEI} and R_{ct} are both within the same order of magnitude for all three electrolytes at 23 °C. However, R_{SEI} and R_{ct} increase significantly at −20 °C, with the 1 M $LiPF_6$-2MeTHF electrolyte showing an acceptable increase, while the other two electrolytes show much higher resistance at different stages, especially R_{SEI} (*SI Appendix*, Fig. S11 *D*–*F* and Table S5). At 23 °C, the simulations show that the Gr||Li half-cell delivers excellent capacity under lithiation at 0.2 C with minimal differences among the three electrolytes (Fig. 4*B*). The simulation results are consistent with the experimental lithiation voltage profiles of all three electrolytes (Fig. 4*B*). The relatively low and comparable R_{SEI} at 23 °C of the three electrolytes results in minor losses across the SEI, causing minimal capacity difference. In contrast, when simulating graphite lithiation at −20 °C, a striking difference in capacity between the electrolytes is observed (Fig. 4*C*). The graphite cycled using 1 M LiFSI-2MeTHF and 1 M $LiPF_6$-2MeTHF+2vol.% FEC electrolytes exhibit very low usable capacities, while cycling in the 1 M $LiPF_6$-2MeTHF electrolyte delivers a specific capacity of 342 mAh g^{-1} even at low temperatures. Fig. 4*D* displays the potential drop across the SEI for the graphite surfaces at the end of lithiation at −20 °C. The comparatively low R_{SEI} of 1 M $LiPF_6$-2MeTHF results in an average potential drop of 37.5 mV, while an order of magnitude higher losses of 351 and 465 mV are observed for 1 M LiFSI-2MeTHF and 1 M $LiPF_6$-2MeTHF+2vol.% FEC, respectively. Although the temperature-dependent ionic conductivities and diffusion coefficients of each electrolyte are included in the computational model, the potential drop across the SEI forms the predominant contributing factor to electrolyte

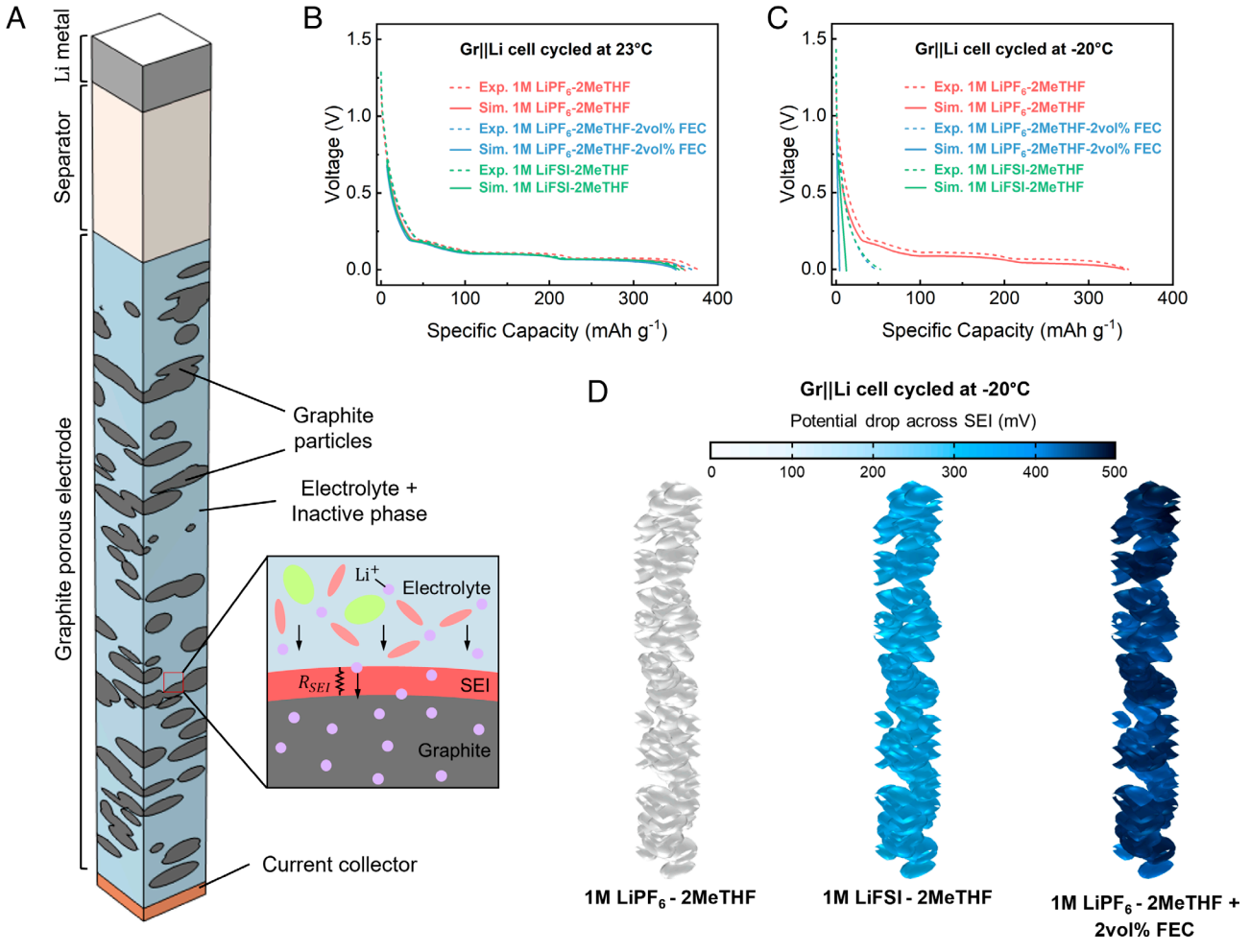

Fig. 4. Modeling simulates intercalation barriers for Li-ion transport in different SEI layers. (*A*) Schematic of Gr||Li cell computational model cycled with the three electrolytes (1 M $LiPF_6$-2MeTHF, 1 M $LiPF_6$-2MeTHF+2vol.% FEC, and 1 M LiFSI-2MeTHF). (*B* and *C*) Experimental and simulated voltage profiles of Gr||Li cell cycled at 0.2 C in the three electrolytes at 23 °C (*B*) and −20 °C (*C*). (*D*) Contour plot of the potential drop on graphite surfaces for the three electrolytes when cycled at 0.2 C at −20 °C.

performance, indicating that the superior performance of 1 M $LiPF_6$-2MeTHF is a consequence of its improved SEI structure.

The deep potential MD (DeePMD) simulations conducted by Hu et al. demonstrate that the massive precipitation of pure LiF bulk phases/grains leads to an extremely low Li ion diffusivity (26), which is also confirmed by other researchers (31, 32). Adjusting the relative contents of LiF versus Li_2CO_3 might be critical to the batteries' rate capability (26, 27). Alternatively, the formation of disordered or nanocrystalline LiF increases Li-ion diffusivity (20, 33, 34). These simulations explain our observation of suppressed Li-ion intercalation in 1 M LiFSI-2MeTHF and 1 M $LiPF_6$-2MeTHF+2vol.% FEC electrolytes. These results strongly suggest that excessive LiF accumulation is responsible for impeding Li-ion transport at low temperatures. The LiF-rich SEI layer cannot help with the Li-ion transport.

Electrochemical Performance. We then systematically test the cell's performance under extreme conditions, specifically fast charging at low temperatures using the 1 M $LiPF_6$-2MeTHF electrolyte. Notably, the Gr||Li cell exhibits outstanding rate performance and cycling stability at room temperature, as depicted in Fig. 2*B*. Even at −20 °C, the Gr||Li cell's performance remains exceptional. At current rates of 0.2, 0.5, 1.0, 2.0, and 3.0 C with 1 C = 0.37 A g^{-1}, the cell delivers 340, 318, 266, 151, and 80 mAh g^{-1}, respectively. After returning to 1.0 C, the Gr anode maintains the same capacity without fading after 500 cycles, with the average Coulombic

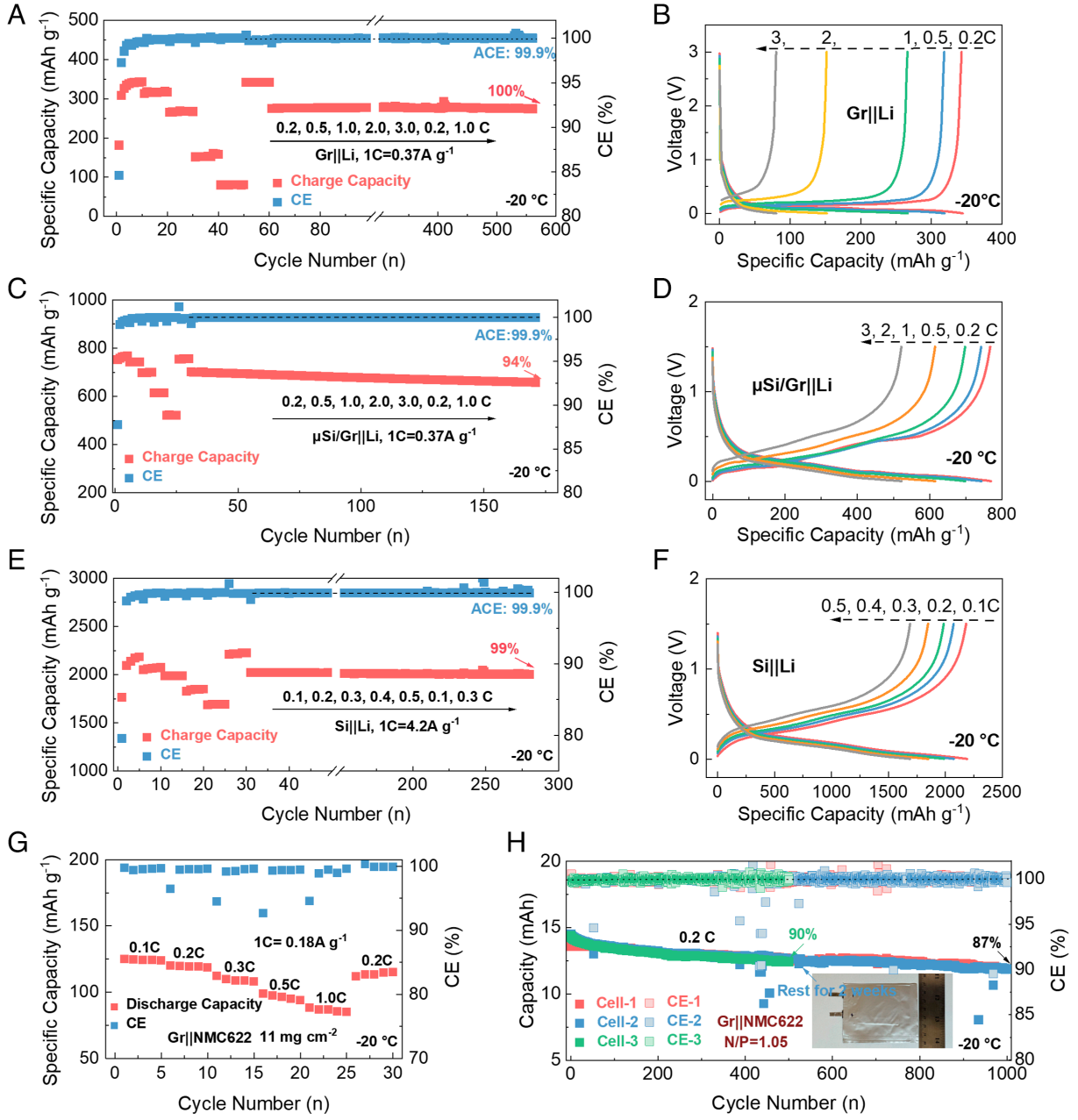

Fig. 5. Electrochemical performance. (*A*) The electrochemical performance of the Gr||Li cell at 0.2 to 3 C (1 C = 0.37 A g^{-1}) and then continuously cycled at 1 C. The breakpoint in the curve is 100 to 300 cycles. (*B*) The voltage profile of the Gr||Li cell. (*C*) The electrochemical performance of the μSi/Gr||Li cell at 0.2 to 3 C (1 C = 0.37 A g^{-1}) and then continuously cycled at 1 C. (*D*) The voltage profile of the μSi/Gr||Li cell. (*E*) The electrochemical performance of the Si||Li cell at 0.1 to 0.5 C (1 C = 4.2 A g^{-1}) and then continuously cycled at 0.3 C. The breakpoint in the curve is 50 to 150 cycles. (*F*) The voltage profile of the Si||Li cell. (*G*) The rate performance of the Gr||NMC622 cell. (*H*) The long-term cycling of the Gr||NMC622 cell at 0.2 C (1 C = 0.18 A g^{-1}). For the Gr||Li, μSi/Gr||Li, and Si||Li cells, discharge and charge are both performed at −20 °C. For the Gr||NMC622 pouch cell, only the 1st charge is performed at room temperature, and then the subsequent charge and discharge cycles are all conducted at −20 °C.

efficiency (ACE) reaching an impressive 99.9% (Fig. 5 *A* and *B*). Another fresh Gr||Li cell stably endures 1,000 cycles at 2.0 C with a remarkable capacity retention of 96%, further highlighting the low-temperature fast-charging capability of our electrolyte (*SI Appendix*, Fig. S12). Additionally, we extend our electrolyte to other anodes such as μSi/Gr and Si anodes), which also demonstrate good low-temperature fast charging performance (Fig. 5 *C*–*F*). As shown in Fig. 5 *C* and *D*, the μSi/Gr anode exhibits high specific capacities of 767, 742, 698, 614, and 521 mAh g^{-1} at 0.2, 0.5, 1.0, 2.0, and 3.0 C (1 C = 0.37 A g^{-1}), respectively. Further cycling at 1.0 C results in 94% capacity retention after 150 cycles for the μSi/Gr anode and an average Coulombic efficiency of 99.9%. A remarkable low-temperature cycling performance is achieved for the pure Si anode. The rate capacities of the Si anode at 0.1, 0.2, 0.3, 0.4, and 0.5 C (1 C = 4.2 A g^{-1}) are 2,182, 2,064, 1,985, 1,846, and 1,689 mAh g^{-1} at −20 °C, respectively (Fig. 5 *E* and *F*). Returning to 0.3 C, the Si anode still maintains a capacity of 2,000 mAh g^{-1} and can be cycled stably 250 times without any capacity decay. The average Coulombic efficiency is 99.9%. Such excellent cycling stability and high capacity of these anodes at low temperatures are truly remarkable. A single-layer pouch cell configuration with Gr anode and NMC622 cathode is cycled at −20 °C. Fig. 5*G* shows the good performance of the Gr||NMC622 cell with specific capacities of 125, 120, 105, 100, and 90 mAh g^{-1} at 0.1, 0.2, 0.3, 0.5, and 1.0 C (1 C = 0.18 A g^{-1}) at −20 °C, respectively (*SI Appendix*, Fig. S13). At 0.2 C, the pouch cell can cycle stably for more than 365 d, achieving capacity retention of 90% after 500 cycles and 87% after 1,000 cycles, respectively (Fig. 5*H* and *SI Appendix*, Fig. S14). Another pouch cell had a 2-wk rest after 500 cycles and then continued to cycle, which ultimately maintained the capacity retention after 1,000 cycles (Fig. 5*H*, blue curve), demonstrating good calendar life during the rest period. Overall, the designed electrolyte derives a dispersed fluorinated SEI that is exceptionally stable and efficiently operates LIBs reversibly. Compared to traditional fluorine-rich SEI, the dispersed fluorinated SEI can enhance Li-ion transport and promote LIBs to deliver excellent rate performance under extreme conditions.

Conclusion

In this work, three representative electrolytes are selected to investigate the roles of SEI in the low-temperature, fast-charging Li-ion batteries. Interestingly, electrolytes with similar desolvation capabilities and SEI compositions show significant variations in performance under extreme conditions, indicating that the microstructure of "fluorinated interphase" is essential. Although the temperature-dependent ionic conductivities and diffusion coefficients of each electrolyte are included in our physics-based finite element simulations, the potential drop across the SEI forms the predominant contributing factor to electrolyte performance. The 1 M $LiPF_6$-2MeTHF electrolyte exhibits the best low-temperature and fast-charging performance, as it forms a thin SEI layer with dispersed small LiF aggregates, which reduces the Li-ion transport energy barrier. We show that such an SEI results in a minimal potential drop across the SEI at low temperatures. Including the FEC additive and changing the Li salt to LiFSI both result in a substantial buildup of LiF, which impedes Li-ion transport through the SEI. The 1 M $LiPF_6$-2MeTHF electrolyte is anode-agnostic and enables outstanding rate capability and fast charging across various anodes (Gr, μSi/Gr, and Si). Pouch cells with $LiNi_{0.6}Mn_{0.2}Co_{0.2}O_2$ cathode exhibit remarkable cycling stability over 1,000 cycles, excellent rate capability at −20 °C, and good calendar life. This understanding of the SEI microstructure provides a highly practical and feasible rationale for the design of Li-ion batteries cycling under extreme conditions.

Materials and Methods

Materials. Graphite, microsilicon graphite, and nano silicon electrode laminates were provided by Argonne National Lab's CAMP Facility and Advano Inc. $LiPF_6$ and LiFSI salts were purchased from Gotion Inc., while 2MeTHF solvent (anhydrous, ≥ 99%, inhibitor-free) was purchased from Fisher Scientific. Solvents were treated with activated molecular sieves to remove moisture, and salts were dried in the glovebox before use.

Cell Assembly and Testing. Electrode laminates were punched into φ12.7 mm disks and vacuum-dried at 120 °C overnight. The electrolyte was 1 M $LiPF_6$-2MeTHF, with two variations for comparison: 1 M $LiPF_6$-2MeTHF+2vol.% FEC and 1 M LiFSI-2MeTHF. Half-cells were assembled in an Ar-filled glovebox with the electrode, 60 μL electrolyte, Celgard2325 separator, and Li foil. Full cells used NMC622 cathode, 60 μL electrolyte, Celgard2325 separator, and fresh Gr anode. Battery testing was performed at room and low temperatures using a NEWARE system.

Electrochemical Measurements. CV measurements were conducted at 0.2 mV s^{-1} using a Princeton VersaSTAT 4 at room temperature. EIS measurements were recorded for the Gr||Li cell during lithiation and delithiation at 23 and −20 °C. Temperature-dependent EIS was tested from 23 to −20 °C using fully lithiated Gr anodes. Activation energies were calculated from the Arrhenius equations by fitting the temperature-dependent resistances:

$$\frac{1}{R(ct,SEI)} = A_0 e^{-\frac{E_a}{RT}},$$

where A_0 is the pre-exponential constant, R is the standard gas constant, and E_a represents the activation energy.

The ionic conductivity of electrolytes was measured using stainless steel (SS) symmetric cells, assembled by sandwiching a 25 μm Celgard2325 separator between φ15.8 mm SS electrodes. The cells were flooded with electrolytes and rested overnight before testing. EIS was recorded over a frequency range of 1 Hz to 1 MHz. The ionic conductivity was calculated using

$$\sigma = \frac{d}{R_b \times S},$$

where d is the separator thickness, R_b is the bulk resistance from Nyquist plots, and S is the SS surface area.

Characterization. After cycling in different electrolytes, SEI layers on the Gr anode were observed using an FEI Talos F200X cryo-TEM equipped with a Gatan cryotransfer holder at liquid nitrogen temperature. Cycled Gr||Li cells were disassembled in the glove box, and the Gr electrodes were peeled off and washed with 2MeTHF to remove residual salts. The washed electrodes were dispersed in 2MeTHF, and the suspension was dropped onto Cu TEM grids. Samples were sealed, transported, and loaded into the cryo-TEM holder under liquid nitrogen conditions to avoid contamination. FTIR spectra of the electrolytes were recorded using a Nexus 670 FTIR spectrometer. Raman measurements were performed on a Horiba Jobin-Yvon using a 532 nm laser. ToF-SIMS measurements were performed on a PHI nanoTOF II with a Bi^+ source, using Ar^+ ion sputtering (3 keV, 100 nA) for the depth profile in a 400 × 400 $μm^2$ area. AFM and nanoindentation were measured using a Dimension Icon AFM (Bruker Nano) in an argon-filled glovebox with H_2O and O_2 levels ≤ 0.1 ppm.

Computational Method. All-atom MD simulations were conducted using LAMMPS) (35) with the OPLS-AA force field (36) to describe atomic interactions. Force field parameters and 1.14 CM1A-LBCC charges were generated using the LigParGen web server (37). To account for polarization effects in a mean-filed sense, charges on ions were scaled by 0.8. This method has been a common practice for better describing the transport properties of electrolytes using non-polarizable force fields (38, 39). Geometry optimization and vibrational frequency calculations were performed in Gaussian16 with the B3LYP/6-311G(d) functional and basis set. For solvation structure calculation, 1,000 2-Methyltetrahydrofuran (2MeTHF) solvent molecules, 100 Li^+, and 100 anions (PF^-_6 or FSI^-) were randomly placed in the simulation box measuring 60^3 Ã…^{3} using Packmol (40) without overlap, corresponding to 1 M $LiPF_6$-2MeTHF and 1 M LiFSI-2MeTHF,

respectively. An additional 28 FEC molecules were added to the 1 M $LiPF_6$–2MeTHF for 2vol.% FEC. Energy minimization of the starting configurations was performed via the conjugate gradient algorithm, followed by relaxation under the isothermal–isobaric (NPT) ensemble at 296 K and 1.0 atm for 0.5 ns. Simulated annealing was carried out for five cycles to overcome the energy barrier of structural relaxation and escape from local minima. The annealing protocol involves a temperature increase from 296 to 500 K over 0.5 ns, a temperature plateau at 500 K for 0.5 ns, a temperature decreases from 500 to 296 K in 0.5 ns, and another temperature plateau at 296 K. The systems were finally equilibrated at 296 K and 1.0 atm under an NPT ensemble for 0.5 ns. The atomistic models of electrolytes at low temperatures, i.e., 253 K were constructed with the same procedures. Three-dimensional (3D) periodic boundary conditions (PBCs) were applied during MD simulations. Long-range electrostatic interactions were computed with the particle–particle particle–mesh (PPPM) method (41) with a cutoff distance of 12 Å. The dielectric constant was set as 6.97. RDFs and cumulative CNs were calculated in LAMMPS. Statistical analysis of solvation structure and visualization were performed with customized MATLAB code and OVITO, respectively.

Finite Element Simulations. Finite element simulations on 3D Li||Gr half-cells were conducted in COMSOL Multiphysics. Electron conduction through the conductive matrix and ionic transport in the liquid electrolyte across the separator and via the porous matrix are defined with the Newman model (29, 42). Plate-like ellipsoidal graphite particles are defined explicitly and randomly distributed within the porous matrix. The a and b principal semiaxes of the graphite particles vary between 0.75 and 2.5 μm, while the c semiaxis along the thickness direction varies between 0.3 and 0.85 μm. The electrode thickness, porosity, mass loading, and active/inactive components' mass fractions are matched with the graphite electrodes prepared for experimental characterization (*SI Appendix*, Table S2). The electrochemical processes occurring in the graphite electrode are coupled with mechanics, including diffusion-induced volume expansion and stresses and stress-assisted Li migration (43, 44). The Larche-Cahn chemical potential defines the thermodynamic driving force for the diffusion of Li within graphite particles. Nonlinear volume changes induced by Li intercalation are modeled analogous to thermal strains. Mismatch strains caused by gradients in Li concentration induce stress in the active material. Conversely, stresses in graphite alter the chemical potential, thereby influencing diffusion kinetics.

$$\mu = \mu_0 + RT\, ln\left(\frac{c}{c_{max} - c}\right) - \Omega\sigma_h,$$

where μ is the chemical potential, μ_0 is the reference potential, R and T are the universal gas constant and absolute temperature, respectively, c is the concentration on Li, c_{max} is the theoretical maximum concentration, Ω is the partial molar volume of Li in graphite, and σ_h is the hydrostatic stress. A linear elastic material model is implemented for graphite and the surrounding matrix with a small strain assumption. The interfacial charge transfer reaction at the graphite–electrolyte interface is defined with the Butler–Volmer equation:

$$i = i_0\left(e\left(\frac{\alpha_a F\eta}{RT}\right) - exp\left(\frac{-\alpha_c F\eta}{RT}\right)\right),$$

where i is the local charger transfer current density, i_0 is the exchange current density, α_a and α_c and the anodic and cathodic transfer coefficients, and F is the Faraday constant. The driving force for the charge transfer reaction is the surface overpotential η The SEI layer formed at the interface impedes the interfacial charge transfer reaction. This role of SEI is included as a surface resistance R_{SEI}, which alters the overpotential as follows:

$$\eta = \phi_c - \phi_1 - E_{eq} - iR_{SEI},$$

where ϕ_c and ϕ_1 are conductive matrix and electrolyte potentials, respectively, and E_{eq} is the equilibrium potential. R_{SEI} is characterized by using EIS at varying SOCs, for each electrolyte, at room temperature and low temperature. Simulations for galvanostatic charging at 0.2 C are conducted for each of the three electrolytes at 23 °C and −20 °C by applying a constant current density at the current collector. The electrolyte ionic conductivity (*SI Appendix*, Fig. S3*A*), diffusion coefficient (*SI Appendix*, Fig. S2 *B* and *C*), and equilibrium voltage (*SI Appendix*, Fig. S10) are updated based on electrolyte selection and temperature in each simulation case.

Data, Materials, and Software Availability. All study data are included in the article and/or *SI Appendix*.

ACKNOWLEDGMENTS. The information, data, or work presented herein was funded in part by the Advanced Research Projects Agency-Energy, US Department of Energy, under Award No. DE-AR0001725. The views and opinions of authors expressed herein do not necessarily state or reflect those of the United States Government or any agency thereof. This research used electron microscopy resources of the Center for Functional Nanomaterials, which is a US Department of Energy Office of Science User Facility, at Brookhaven National Laboratory under Contract No. DE-SC0012704. S.R.S., X.Y., and K.Z. acknowledge the support by the NSF through the Grants CMMI-2210158 and CBET-2349666. J.L., Y.G., and F.S. thank the support from the US Department of Energy under Contract DE-NE0009286 and the NSF under Grant No. 2239690. H.Z. and F.S. were partially supported by the Assistant Secretary for Energy Efficiency and Renewable Energy, Office of Vehicle Technologies of the US Department of Energy through the Advanced Battery Materials Research Program. We acknowledge cell analysis, modeling, and prototyping for supplying graphite powder and electrodes. We also thank Dr. Feng Xu from the University of Delaware for performing Time of Flight Secondary Ion Mass Spectrometry (ToF-SIMS) characterization. This characterization was performed with the instrument sponsored by the NSF under Grant No. DMR-2116754.

Author affiliations: [a]Department of Chemistry, Virginia Tech, Blacksburg, VA 24061; [b]Department of Energy and Mineral Engineering, Pennsylvania State University, University Park, PA 16802; [c]School of Mechanical Engineering, Purdue University, West Lafayette, IN 47907; [d]Micron School of Materials Science and Engineering, Boise State University, Boise, ID 83725; [e]Center for Functional Nanomaterials, Brookhaven National Laboratory, Upton, NY 11973; [f]Macromolecules Innovation Institute, Virginia Tech, Blacksburg, VA 24061; and [g]Department of Materials Science and Engineering, Virginia Tech, Blacksburg, VA 24061

Author contributions: L.T. and F.L. designed research; L.T., H.Z., S.R.S., X.Y., J.L., Y.G., J.A.R., D.X., J.M., W.H., C.S., Z.L., D.Y., S.H., and F.L. performed research; L.T., H.Z., S.R.S., X.Y., J.L., H.X., L.A.M., K.Z., F.S., and F.L. analyzed data; and L.T., S.R.S., K.Z., F.S., and F.L. wrote the paper.

1. C. Y. Wang *et al.*, Fast charging of energy-dense lithium-ion batteries. *Nature* **611**, 485–490 (2022).
2. D. Hubble *et al.*, Liquid electrolyte development for low-temperature lithium-ion batteries. *Energy Environ. Sci.* **15**, 550–578 (2022).
3. N. Zhang *et al.*, Critical review on low-temperature Li-ion/metal batteries. *Adv. Mater.* **34**, 2107899 (2022).
4. M. T. F. Rodrigues *et al.*, A materials perspective on Li-ion batteries at extreme temperatures. *Nat. Energy* **2**, 17108 (2017).
5. Y. S. Meng, V. Srinivasan, K. Xu, Designing better electrolytes. *Science* **378**, 3750 (2022).
6. Y. Liu, Y. Zhu, Y. Cui, Challenges and opportunities towards fast-charging battery materials. *Nat. Energy* **4**, 540–550 (2019).
7. H. Cheng *et al.*, Emerging era of electrolyte solvation structure and interfacial model in batteries. *ACS Energy Lett.* **7**, 490–513 (2022).
8. D. Xia *et al.*, Design criteria of dilute ether electrolytes toward reversible and fast intercalation chemistry of graphite anode in Li-ion batteries. *ACS Energy Lett.* **8**, 1379–1389 (2023).
9. L. Tao *et al.*, Reversible switch in charge storage enabled by selective ion transport in solid electrolyte interphase. *J. Am. Chem. Soc.* **145**, 16538–16547 (2023).
10. Y. Yao *et al.*, Unlocking charge transfer limitations for extreme fast charging of Li-ion batteries. *Angew. Chem.* **135**, e202214828 (2023).
11. K. Xu, "Charge-transfer" process at graphite/electrolyte interface and the solvation sheath structure of Li^+ in nonaqueous electrolytes. *J. Electrochem. Soc.* **154**, A162 (2007).
12. S. Weng *et al.*, Temperature-dependent interphase formation and Li^+ transport in lithium metal batteries. *Nat. Commun.* **14**, 4474 (2023).
13. S. S. Zhang, Design aspects of electrolytes for fast charge of Li-ion batteries. *InfoMat* **3**, 125–130 (2021).
14. Y. Zhang *et al.*, Electrolyte design for lithium-ion batteries for extreme temperature applications. *Adv. Mater.* **36**, 2308484 (2024).
15. Y. X. Yao *et al.*, Regulating interfacial chemistry in lithium-ion batteries by a weakly solvating electrolyte. *Angew. Chem. Int. Ed.* **60**, 4090–4097 (2021).
16. Y. Yang *et al.*, Synergy of weakly-solvated electrolyte and optimized interphase enables graphite anode charge at low temperature. *Angew. Chem. Int. Ed.* **61**, e202208345 (2022).
17. H. Wan, J. Xu, C. Wang, Designing electrolytes and interphases for high-energy lithium batteries. *Nat. Rev. Chem.* **8**, 30–44 (2023).
18. J. Xu *et al.*, Electrolyte design for Li-ion batteries under extreme operating conditions. *Nature* **614**, 694–700 (2023).
19. L. Wang *et al.*, Identifying the components of the solid–electrolyte interphase in Li-ion batteries. *Nat. Chem.* **11**, 789–796 (2019).
20. A. Dopilka, J. M. Larson, H. Cha, R. Kostecki, Synchrotron near-field infrared nanospectroscopy and nanoimaging of lithium fluoride in solid electrolyte interphases in Li-ion battery anodes. *ACS Nano* **18**, 15270–15283 (2024).
21. G. M. Hobold, C. Wang, K. Steinberg, Y. Li, B. M. Gallant, High lithium oxide prevalence in the lithium solid–electrolyte interphase for high Coulombic efficiency. *Nat. Energy* **9**, 580–591 (2024).

22. S. Tan *et al.*, Evolution and interplay of lithium metal interphase components revealed by experimental and theoretical studies. *J. Am. Chem. Soc.* **146**, 11711–11718 (2024).
23. L. Huang *et al.*, Insight into the role of fluoroethylene carbonate in solid electrolyte interphase construction for graphite anodes of lithium-ion batteries. *J. Phys. Chem. C* **128**, 9586–9594 (2024).
24. J. Tan, J. Matz, P. Dong, J. Shen, M. Ye, A growing appreciation for the role of LiF in the solid electrolyte interphase. *Adv. Energy Mater.* **11**, 2100046 (2021).
25. N. Qin *et al.*, Trace $LiBF_4$ enabling robust LiF-rich interphase for durable low-temperature lithium-ion pouch cells. *ACS Energy Lett.* **9**, 4843–4851 (2024).
26. T. Hu *et al.*, Impact of the local environment on Li ion transport in inorganic components of solid electrolyte interphases. *J. Am. Chem. Soc.* **145**, 1327–1333 (2023).
27. Y.-H. Tan *et al.*, Inorganic composition modulation of solid electrolyte interphase for fast charging lithium metal batteries. *Adv. Mater.* **36**, 2404815 (2024).
28. D. Yu *et al.*, Uncorrelated lithium-ion hopping in a dynamic solvent-anion network. *ACS Energy Lett.* **8**, 1944–1951 (2023).
29. K. Xu, Y. Lam, S. S. Zhang, T. R. Jow, T. B. Curtis, Solvation sheath of Li^+ in nonaqueous electrolytes and its implication of graphite/electrolyte interface chemistry. *J. Phys. Chem. C* **111**, 7411–7421 (2007).
30. B. Nan *et al.*, Graphite lithium-ion batteries at low temperatures by using low-polarity-solvent electrolytes. *Angew. Chem. Int. Ed.* **61**, e202205967 (2022).
31. H. Yildirim, A. Kinaci, M. K. Y. Chan, J. P. Greeley, First-Principles analysis of defect thermodynamics and ion transport in inorganic SEI compounds: LiF and NaF. *ACS Appl. Mater. Interfaces* **7**, 18985–18996 (2015).
32. L. Benitez, J. M. Seminario, Ion diffusivity through the solid electrolyte interphase in lithium-ion batteries. *J. Electrochem. Soc.* **164**, 3159 (2017).
33. C. Li, L. Gu, J. Maier, Enhancement of the Li conductivity in LiF by introducing glass/crystal interfaces. *Adv. Funct. Mater.* **22**, 1145–1149 (2012).
34. L. Alzate-Vargas, K. S. N. Vikrant, S. Allu, J. L. Fattebert, Atomistic modeling of LiF microstructure ionic conductivity and its influence on nucleation and plating. *Phys. Rev. Mater.* **6**, 095402 (2022).
35. A. P. Thompson *et al.*, LAMMPS–A flexible simulation tool for particle-based materials modeling at the atomic, meso, and continuum scales. *Comput. Phys. Commun.* **271**, 108171 (2022).
36. G. A. Kaminski, R. A. Friesner, J. Tirado-Rives, W. L. Jorgensen, Evaluation and reparametrization of the OPLS-AA force field for proteins via comparison with accurate quantum chemical calculations on peptides. *J. Phys. Chem. B* **105**, 6474–6487 (2001).
37. L. S. Dodda, I. C. De Vaca, J. Tirado-Rives, W. L. Jorgensen, LigParGen web server: An automatic OPLS-AA parameter generator for organic ligands. *Nucleic Acids Res.* **45**, W331–W336 (2017).
38. V. Chaban, Polarizability versus mobility: Atomistic force field for ionic liquids. *Phys. Chem. Chem. Phys.* **13**, 16055–16062 (2011).
39. B. Doherty, X. Zhong, S. Gathiaka, B. Li, O. Acevedo, Revisiting OPLS force field parameters for ionic liquid simulations. *J. Chem. Theory Comput.* **13**, 6131–6135 (2017).
40. L. Martinez, R. Andrade, E. G. Birgin, J. M. Martínez, PACKMOL: A package for building initial configurations for molecular dynamics simulations. *J. Comput. Chem.* **30**, 2157–2164 (2009).
41. R. W. Hockney, J. W. Eastwood, *Computer Simulation Using Particles* (CRC Press, 2021), 10.1201/9780367806934.
42. J. Newman, N. Balsara, *Electrochemical Systems* (Wiley, 2021).
43. S. R. Shah, L. S. De Vasconcelos, K. Zhao, Computational modeling of electrochemomechanics of high-capacity composite electrodes in Li-ion batteries. *J. Appl. Mech.* **89**, 081005 (2022).
44. L. S. De Vasconcelos *et al.*, Chemomechanics of rechargeable batteries: Status, theories, and perspectives. *Chem. Rev.* **122**, 13043–13107 (2022).